Investigation of Inclusion Removal at Steel–Slag Interface toward a Small-Scale Criterion for Particle Separation

Xiaomeng Zhang, Stefan Pirker, and Mahdi Saeedipour**

Interactions between inclusion particles and the steel–slag interface directly affect the inclusion removal efficiency and thus influence steel cleanliness. Herein, the three-phase interactions are resolved using the volume of fluid (VOF) method coupled with a dynamic overset mesh. The simulation is able to capture the instantaneous interface deformation and predict the particle motion driven by capillary force. The model validity is first demonstrated by comparison with analytical results. Then, a parameter study is conducted to examine the most influential factors governing the separation process. The results show that the system's wetting condition and the slag viscosity have a decisive effect on particle behavior at the interface (separation or entrapment). From an energy perspective, a better wetting condition generates more energy sources, and the interfacial energy is efficiently transformed into the particle's kinetic energy within a less viscous environment, thus leading to better separation. Besides, a criterion for predicting particle behavior is developed based on a modified Reynolds number (Re_γ, relevant to fluid properties) and a quantity related to particle dynamics (ζ). The current work brings insights into the interfacial phenomenon during inclusion removal, which can be incorporated into large-scale simulations to estimate the removal efficiency more accurately.

1. Introduction

Nonmetallic inclusions are an inevitable component of the steel melt and typically exist in the form of various oxides and nitrides, which could deteriorate the mechanical properties of steel and cause nozzle clogging during continuous casting.[1,2] Lowering the amount of inclusion in molten steel by slag absorption is always a critical and fundamental aspect of steel cleanliness control. The inclusion removal process is recognized as containing three stages: 1) transport of inclusions to the steel–slag interface, 2) movement after impacting the interface, and 3) subsequent or simultaneous dissolution in the slag.[3–5] As inclusions are less dense than steel, they can rise toward the melt surface due to buoyancy. Different flow control strategies like installing flow control devices[6] and gas injection[7] assist that as well. As for dissolution, the steelmaking slags readily dissolve the most common inclusions, and there have been many efforts in the characterization of dissolution mechanisms.[8–10] In comparison, the intermediate stage is not given enough attention and remains the least understood part of the whole removal process. The steel–slag interface has been well reported as an important site where many interfacial phenomena take place, for instance, agglomeration of inclusion particles at steel–slag interfaces,[11] chemical reactions between liquid-iron alloys and liquid slags and associated dynamic interfacial phenomena (i.e., the Marangoni convection)[12] as well as interacting with the main flow in the vicinity of the interface.[13,14] Hence, the interfacial phenomenon controlling inclusion removal should also be emphasized and better understood. It could help to prevent the re-entrainment of inclusions and facilitate subsequent dissolution, thus giving better control of steel cleanliness.

There have been relatively few studies on inclusion transfer at the steel–slag interface. As one of the earliest studies, Nakajima and Okamura[15] proposed a mathematical model which has become the basis for most follow-up work. This model conducts a force analysis for the particle in the vicinity of the steel–slag interface, taking the buoyancy, drag, and fluid added mass forces as well as the interfacial force into account. Accordingly, particle motion is determined by Newton's second law. Three situations exist based on the particle's displacement: passing the interface, staying, and oscillating at the interface. The model considers that the fluid interface remains flat throughout the separation process, leading to the main drawback as a less accurate estimation of the capillary force. Based on Nakajima's model, Bouris et al.[16] further investigated the re-entrainment of trapped inclusions from the steel–slag interface by considering the effect of a turbulent boundary layer near the interface. Shannon et al.[17] expanded the model to study the separation of inclusion with different shapes at various slag conditions. The dissolution of

X. Zhang
K1-MET GmbH
Stahlstrasse 14, 4020 Linz, Austria
E-mail: xiaomeng.zhang@jku.at

X. Zhang, S. Pirker, M. Saeedipour
Department of Particulate Flow Modelling
Johannes Kepler University
4040 Linz, Austria
E-mail: mahdi.saeedipour@jku.at

The ORCID identification number(s) for the author(s) of this article can be found under https://doi.org/10.1002/srin.202200842.

DOI: 10.1002/srin.202200842

settled inclusion was also considered by a fundamental kinetic model. Strandh et al.[18,19] conducted a detailed parameter study using this model and proposed the possible application of the model to slag system design. In addition, Liu and Yang et al.[20] considered the change of the drag force under different Reynolds numbers instead of the single Stokes flow given in the original model.

Although the studies mentioned above have made many improvements, the essential assumption remains unchanged: the interface deformation during contact is neglected. Due to the high interfacial tension of the steel–slag interface and the small size of the inclusion particle, the capillary action during the separation is significant. The capillary force manifests different effects and magnitudes according to the meniscus shape, for example, as a support force for water-walking insects at the interface[21] or a retracting force when pulling a particle out of a liquid–fluid interface.[22,23] Neglecting interface deformation will inaccurately estimate the position of the three-phase contact line acting on the particle, thus directly affecting the calculation of the resulting capillary force and particle motion. Apart from the assumption of a flat interface during three-phase interaction, the Nakajima model also assumes the existence of the liquid film ahead of a particle upon the initial contact with the fluid interface in some cases, which is further emphasized by Xuan et al.[24]. Evidence to support this claim seems to mainly come from experimental observations on systems with very low interfacial tension compared to the steel–slag system, such as light mineral oil and water phases (about 30 times smaller).[25] Experiments are sometimes also subjected to relatively large particles, where gravitation usually plays a role. Nevertheless, it is pointed out that the interface deformation caused by an approaching particle increases with the sphere's size and decreases with the interfacial tension as well as the viscosity of fluids.[26–28] It underlines the particularity of the steel–slag interface, which is hardly deformed upon the approach of a small particle but has strong capillary actions while contacting the particle. Although the previous studies concluded the importance of overall wettability on inclusion separation, the mathematical model cannot describe the fundamental phenomenon of meniscus formation and accurately calculate particle motion. By contrast, computational fluid dynamics (CFD) simulations have shown great potential in providing detailed insights into complex multiphase regimes and interfacial phenomena, such as the liquid–gas bubbles flow inside the submerged entry nozzle and slag entrapment into the liquid pool in the continuous casting process.[29–31] Concerning inclusion particle removal at the steel–slag interface, Liu et al.[32] recently studied a solid particle drifting in steel and motion at the interface by a phase-field model. In addition, Zhang et al.[33] concentrated on the three-phase interactions and simulated the particle separation process at the steel–slag interface employing a dynamic mesh technique. More investigations remain necessary to reveal the mechanism regarding interfacial separation.

The present work focuses on the stage of inclusion particle transfer at the steel–slag interface in the removal process. It is intended to be addressed by numerical simulations based on the volume of fluid (VOF) method and a dynamic overset grid, which proves to be effective by comparing with analytical results. The resolved simulations can visualize the particle's motion process and the establishment and transient evolution of a meniscus resulting from the wetting property of the three-phase system. Besides, a parameter study is conducted to examine the factors that control the mechanism and dynamics of the separation stage. On this basis, an attempt is made to develop a general criterion to distinguish particle behavior within different conditions.

The article is structured as follows. In Section 2, the basic scenario of particle–fluid interface interactions is first introduced from an analytical perspective. Then, Section 3 presents the simulation method. The rest of the article concerns the results and interpretation of analytical and numerical calculations.

2. Analytical Considerations

The basic scenario of a small particle positioned at the interface between two immiscible fluids is schematically shown in **Figure 1**. Around the spherical particle, an axisymmetric meniscus forms due to interfacial tension and wettability of fluids. The meniscus meets the solid surface at an angle θ dependent on the particular combination of materials in the given system and approaches a horizontal plane at large distances from the particle.

The profile of such a deformed interface under static equilibrium is governed by the Young–Laplace (Y–L) equation. This equation is essentially a statement of balance between hydrostatic pressure and curvature pressure at the fluid interface, i.e., $\Delta p = -\gamma(\kappa_1 + \kappa_2)$, where Δp is the pressure difference, γ is the interfacial tension, and $\kappa_i (i = 1, 2)$ is the principal curvature. In the case of an axisymmetric interface $z = z(r)$, the Y–L equation reads[34]

$$(\rho_1 - \rho_2) g z = -\gamma \left[\frac{d^2z/dr^2}{[1 + (dz/dr)^2]^{3/2}} + \frac{dz/dr}{r[1 + (dz/dr)^2]^{1/2}} \right] \quad (1)$$

The left side of the equation refers to the hydrostatic pressure and $\rho_i (i = 1, 2)$ is the fluid density. On the right side, it is the curvature pressure or named Laplace pressure, with a negative sign to describe a decurved meniscus as shown in Figure 1. In consideration of a meniscus can develop a neck where the function $z = z(r)$ becomes double-valued for a range of r near the neck, it is more convenient to describe the meniscus as $r = r(z)$. Meanwhile, by using a dimensionless variable $A = \sqrt{(\rho_1 - \rho_2) g/\gamma}$ and defining $y = zA$ and $x = rA$, Equation (1) is converted to

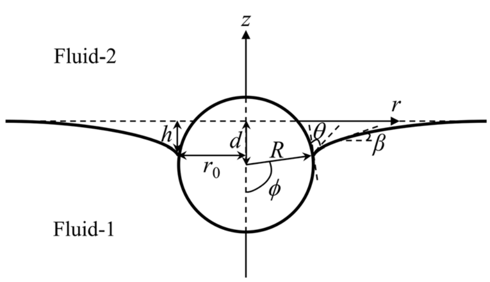

Figure 1. Schematic of particle at a fluid–fluid interface. θ is the three-phase contact angle, ϕ is a central angle that locates the contact line on the particle surface, and the meniscus inclination angle is β. In addition, meniscus height is denoted by h, and the relative position of particle center to the fluid interface is represented by d. Fluid-1 and Fluid-2 may represent water and air, respectively. When referring to a steel–slag system, Fluid-1 is the steel phase, and Fluid-2 is the slag.

$$y = \frac{d^2x/dy^2}{[1+(dx/dy)^2]^{3/2}} - \frac{1}{x[1+(dx/dy)^2]^{1/2}}$$
$$\text{B.C.}: \begin{cases} dx/dy = \cot\beta_0, & \text{at } y = y_0 \\ dx/dy \to \infty \text{ and } x \to \infty, & \text{as } y \to 0 \end{cases} \tag{2}$$

where β_0 is the value of β at the three-phase contact, and y_0 is the dimensionless meniscus height. The solution to the mathematical system yields the profile of the static meniscus. Characterized by a second-order nonlinear differential equation with two boundary conditions, the problem can be numerically solved by the shooting method so that it can be reduced to an initial-value problem.[35] By supplementing a guessed initial value which needs to be adjusted constantly, there is eventually a solution at the other boundary that satisfies the given boundary condition. Specifically, for the current case, the initial conditions are set at the contact point, that are $x(y_0) = Ar_0$ and $x'(y_0) = \cot\beta_0$ with a guessed value y_0. The shooting target is the second boundary condition at the far field, which means the solution $x'(0; y_0)$ for the given y_0 has to satisfy the condition $x'(0; y_0) \to \infty$. As the second boundary is at infinity, it is necessary to be replaced by a point at a finite distance x^* far from the three-phase contact and with negligible deformation. An approximated solution with a small interface inclination is given by

$$y(x) = -K_0(x)/K_1(x^*)\tan\beta^* \tag{3}$$

where $K_i(i = 0, 1)$ is the modified Bessel function of the second kind and ith order.[36] An inclination angle $\beta^* = 0.5 - 1°$ should be sufficient. For more details on solving the Y–L equation by the shooting method, it refers to studies [35,36]. Here, the computing procedure of the shooting method is implemented in MATLAB, and the ode45 solver is used for solving the initial value problem.

Once the meniscus profile is determined, i.e., the contact point and the central angle at the particle surface are known, the resulting capillary force acting on the particle is calculated by the direct action of the interfacial tension at the three-phase contact line (with the length $l = 2\pi R\sin\phi$). The vertical component of the force is given by

$$\mathbf{F}_\sigma = -l\gamma\sin(\theta - \phi) \tag{4}$$

The sign convention implied by this term is adhered to: the upward force is positive (as a driving force for the particle), and the downward force is negative (acting as resistance).

3. Numerical Modeling

The analytical approach above gives a hint of capillary interactions only from a stationary equilibrium point of view, whereas most cases involve dynamic processes. Therefore, numerical simulations are conducted to investigate more realistic situations. The considered system contains two immiscible fluids, and the fluid–fluid interface motion upon the impact of a solid particle needs to be resolved. The VOF method[37] is used for this purpose. The VOF method for incompressible two-phase flow consists of the continuity and Navier–Stokes equations along with a transport equation for phase volume fraction. The whole set of equations read

$$\nabla\cdot\mathbf{U} = 0 \tag{5}$$

$$\frac{\partial(\rho\mathbf{U})}{\partial t} + \nabla\cdot(\rho\mathbf{U}\mathbf{U}) = -\nabla p + \nabla\cdot\boldsymbol{\tau} + \rho\mathbf{g} + \mathbf{F}_\sigma \tag{6}$$

$$\frac{\partial\alpha}{\partial t} + \nabla\cdot(\alpha\mathbf{U}) = 0 \tag{7}$$

where U is the velocity vector shared between the fluids, τ is the stress tensor with the form of $\mu(\nabla\mathbf{U} + \nabla\mathbf{U}^\mathrm{T})$ for Newtonian fluids, p is the pressure field, and the scalar α denotes the volume fraction of fluid. Equation (7) is solved just for one of the two phases, and the sum of the two equals one in each control volume. In addition, α is used to determine the phase-averaged density by $\rho = \alpha\rho_1 + (1-\alpha)\rho_2$, and the viscosity μ is computed in the same manner. $\mathbf{F}_\sigma$ is the surface tension force calculated by the continuum surface force (CSF) approach[38] and reads

$$\mathbf{F}_\sigma = \sigma k\hat{\mathbf{n}}\delta_\mathrm{s} \tag{8}$$

with σ the surface tension coefficient and δ_s a mathematical delta function approximated by $|\nabla\alpha|$ and nonzero in interface cells only. k is the interfacial curvature computed by $k = -\nabla\cdot\hat{\mathbf{n}}$ with the unit normal $\hat{\mathbf{n}} = \nabla\alpha/|\nabla\alpha|$. To include the wetting conditions between the fluid interface and the solid particle, the unit normal vector at cells adjacent to the particle surface is adjusted according to the contact angle θ. It is calculated by $\hat{\mathbf{n}} = \hat{\mathbf{n}}_\mathrm{w}\cos\theta + \hat{\mathbf{t}}_\mathrm{w}\sin\theta$, where $\hat{\mathbf{n}}_\mathrm{w}$ and $\hat{\mathbf{t}}_\mathrm{w}$ are the unit vectors normal and tangential to the wall, respectively.

Once the above governing equations of fluid dynamics are solved, the resulting fluid forces and moments acting on the particle are determined by numerical integrating the pressure and the viscous components over the particle surface. Then the movement of the particle is solved by the six degrees of freedom (6-DOF) solver based on Newton's second law. The particle's translational and angular motion are computed in the inertial coordinate system (indicated by a subscript I) and the body coordinate system (subscript B), respectively. The governing equations for particle motion are written as

$$m\frac{\mathrm{d}\mathbf{u}_\mathrm{I}}{dt} = \sum\mathbf{F}_\mathrm{I} \tag{9}$$

$$\mathbf{I}_\mathrm{B}\frac{\mathrm{d}\boldsymbol{\omega}_\mathrm{B}}{dt} + \boldsymbol{\omega}_\mathrm{B}\times\mathbf{I}_\mathrm{B}\boldsymbol{\omega}_\mathrm{B} = \sum\mathbf{M}_\mathrm{B} \tag{10}$$

where m is the mass of the particle, $\mathbf{u}_\mathrm{I}$ is the linear velocity vector of the center of gravity, and $\sum\mathbf{F}_\mathrm{I}$ is the sum of all forces on the particle in which the gravity and contributions from the buoyancy, drag, added mass forces, and the capillary force are included. For the angular motion equation, $\mathbf{I}_\mathrm{B}$ is the moment of inertia matrix, $\boldsymbol{\omega}_\mathrm{B}$ is the rigid body angular rotation vector, and $\mathbf{M}_\mathrm{B}$ is the moment vector of the object. The moments are transformed from inertial to body coordinates by[39]

$$\mathbf{M}_\mathrm{B} = \mathbf{R}\mathbf{M}_\mathrm{I} \tag{11}$$

where R is the transformation matrix. Similarly, the angular velocity is transformed back to the inertial coordinate system via $\boldsymbol{\omega}_\mathrm{I} = \mathbf{R}^\mathrm{T}\boldsymbol{\omega}_\mathrm{B}$. The velocities $\mathbf{u}_\mathrm{I}$ and $\boldsymbol{\omega}_\mathrm{I}$ are used in dynamic mesh calculations to update the particle position, followed by calculating the volume fraction distribution and flow field for the further time step. For more accurate VOF solutions, the volume fraction discretization uses the geometric reconstruction scheme, which presents a sharp interface between fluids by a piecewise-linear approach and is the most accurate option available. Besides, the PRESTO! scheme is used for pressure interpolation, and the first-order schemes in temporal and momentum spatial discretization are applied to ensure the stability of the solution. The CFD software package of ANSYS Fluent is employed for the simulation in this study.

Considering the motion process of a spherical particle driven by capillary force, simulations are conducted in an originally stationary two-fluid domain with the particle initially touching the fluid–fluid interface, as schematically shown in **Figure 2**a. As particle motion and the ambient flow should be symmetric regarding the axis that is through the sphere center and in the direction of motion, the physical configuration is simulated based on a simplified axisymmetric computational domain with wall-boundary restriction on the other sides. A dynamic mesh technique—the overset grid[40]—is used to enable the particle motion, and meanwhile, it is able to maintain good mesh quality and provide more accurate calculations of surface tension effects throughout the process. As displayed in Figure 2b, the whole mesh consists of two parts: the large gray area which is the background mesh and represents the fluid domain and the component mesh around the particle surface. The component mesh is first overlapping on top of the background. After initializing the fluid field, the two sets of mesh integrate into an entirety and are connected by a minimized overlapping region that continuously updates in the course of particle motion. Grid independence is examined by plotting the particle velocity versus its displacement during moving across the fluid interface under various grid resolutions, which is demonstrated in **Figure 3**. The resolution of Grid-1 is set as $0.05R$, where R is the particle radius. Grid-2 and Gird-3 are further refined with a size of $0.025R$ and $0.0125R$, respectively. It can be seen that the three sets of grids result in similar trends. However, the relatively coarse Grid-1

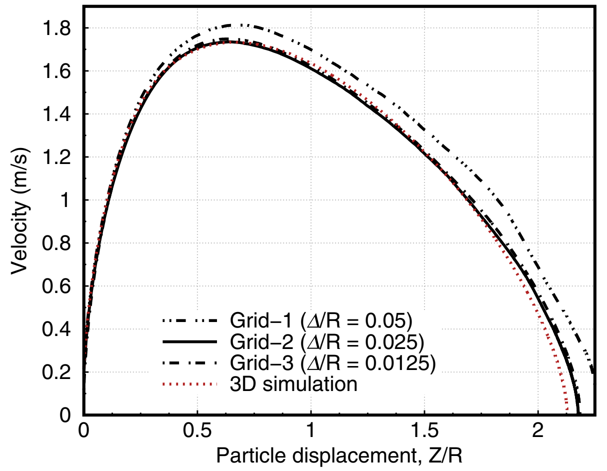

Figure 3. Particle velocity–displacement diagram under three grid resolutions of 2D-axisymmetric simulations and comparison with the result from 3D simulation. Particle displacement Z is normalized with the particle radius R, and symbol Δ denotes the grid size.

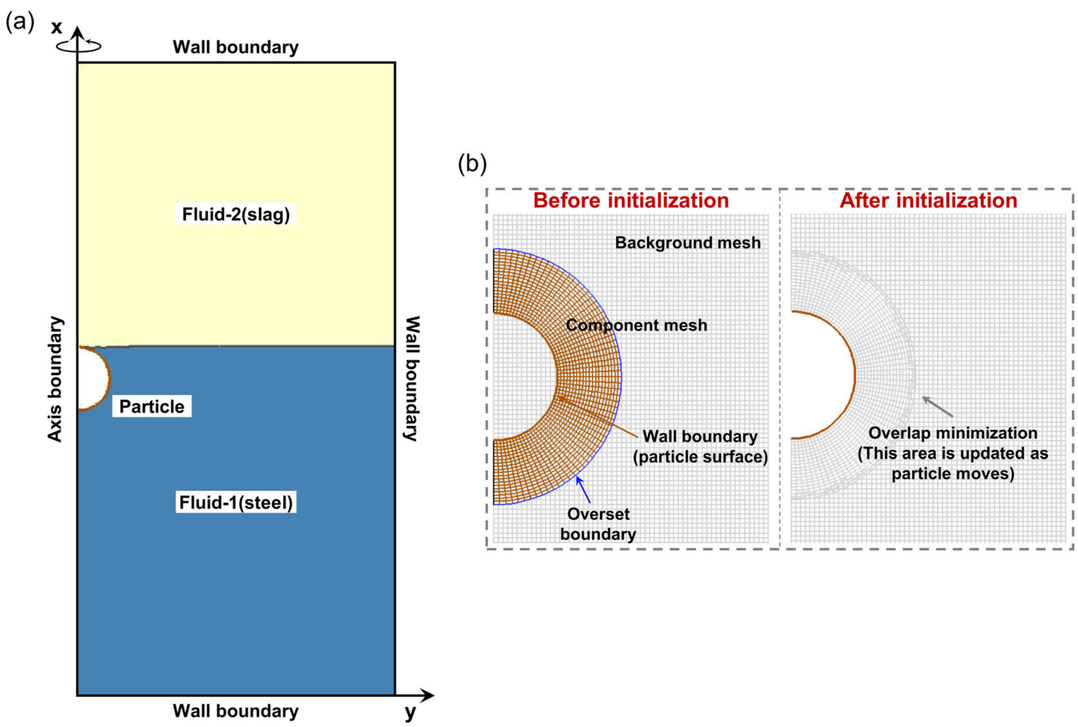

Figure 2. a) Axisymmetric computational domain and boundary conditions; b) schematics of the overset mesh. Left side: independent two parts—background grid and component grid around particle surface before initialization. Right side: grids assembled by the minimized overlapping area after initialization.

leads to an overestimation of the velocity magnitude and the maximum displacement. A further refinement based on Grid-2 gives rise to basically the same results. Moreover, the current results have also been compared with our previous study which is based on full 3D simulations.[33] As can be seen, both results are generally in reasonable agreement except for the minor discrepancy of particle position in the later stage of motion. The maximum relative error from the result by Grid-2 versus 3D simulation is less than 2.3% which should not affect the overall behavior of the particle. Especially, 2D-axisymmetric simulations make a thorough parameter study and the general criterion developing possible (both depend on a large number of case studies) given the high computational expense from all 3D simulations. Therefore, the following simulations are carried out based on Grid-2.

4. Results and Discussion

4.1. Analytical Meniscus Profiles and Comparisons with CFD Simulations

With the introduction in Section 2, solutions to the Y–L equation (Equation (2)) give the meniscus profile at the stationary state for a given three-phase contact angle θ and a central angle ϕ, and the theoretical capillary force acting on the spherical particle in the specific position is obtained by Equation (4). The applicability of the Y–L equation and theoretical considerations in the circumstances where the water–air interface is impacted by a moving sphere has been established by experimental studies.[41–43] For example, water entry of a small sphere in the low Bond number and low Weber number limits reported by Aristoff et al.[42] and the detachment of a particle from the water surface by Pitois.[43] These processes render a quasistatic state. Thus, the meniscus around a moving particle can be described by the Y–L equation. Similar to experiments, we intend to apply the aforementioned numerical model (i.e., the VOF method and the CSF approach) as an additional way to the water-air system. Comparisons between the analytical and simulated results are shown in **Figure 4**. It turns out analytics can be used as a validation of the current numerical model. Besides, it would help to better analyze and understand the inclusion particle behavior at the steel–slag interface. The interaction between the inclusion particle and steel–slag interface will be presented in the following Section 4.2. The parameters of the studied system are listed in **Table 1**.

Figure 4a presents the capillary force acting on the particle as a function of the central angle ϕ in two wetting conditions distinguished by the three-phase contact angle $\theta = 10°$ and 50°. ϕ continuously changes from 180° to 0°, corresponding to the contact of the fluid interface with the particle surface from the top of the particle to the bottom. According to the theoretical force curves, the force increases since the first touch and reaches the maximum at $\phi = \theta/2 + 90°$, that is, 95° and 115° for two conditions. Then, the force starts to decrease and get to the first zero which indicates an equilibrium state assuming a horizontal interface profile at ϕ equal to 10° and 50° ($\phi = \theta$), respectively.

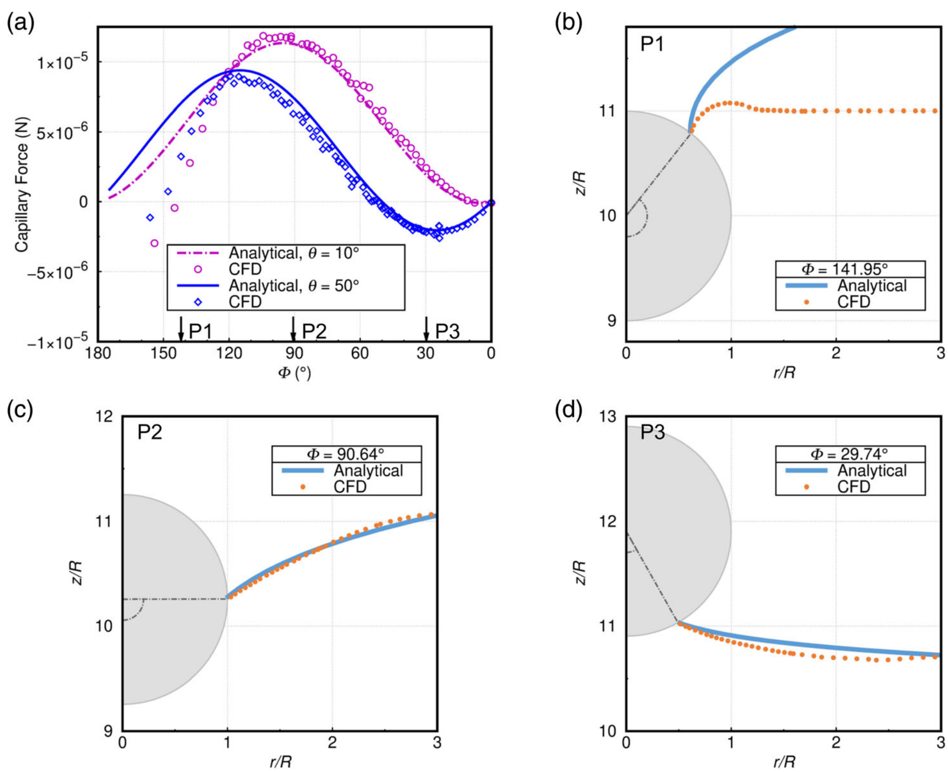

Figure 4. a) Capillary force acting on particle at different location angle ϕ by theoretical calculation and simulation; b–d) meniscus configurations predicted by the Young–Laplace equation and the numerical simulation, corresponding to location P1, P2, and P3 in the top left figure.

Table 1. Parameters involved in the case of a sphere at a water–air interface.

	Density ρ [kgm^{-3}]	Viscosity μ [$Pa \cdot s$]	Interfacial tension σ [Nm^{-1}]	Size [μm]
Water	997	8.949×10^{-4}	0.07275	–
Air	1.29	1.85×10^{-5}		–
Particle	3980	–	–	50

Afterward, the force becomes negative and has the maximum value at 5° and 25° ($\phi = \theta/2$). The force continues to decrease and approaches a second zero as the particle gradually moves away from the interface. The condition with a smaller contact angle possesses a larger positive capillary force, whereas a smaller value in the negative direction, which could provide the particle with more driving force and impose less resistance for particle's upward motion. As for the results obtained by the simulations, they are in general consistent with the analytical results except for forces at the initial stage. Since the dynamic motion of particle starts with touching the interface, the initial period for meniscus formation and establishment especially deviates from the stationary meniscus described by the Y–L equation, which will be further discussed later. Over time the discrepancy has decreased, and the motion can be regarded as a quasistatic process. In addition, it should be noted that the force considered in the simulation is actually the total force acting on the sphere. By comparison with the theoretical capillary force, it indicates that the capillary force is completely dominant for a small particle within the water–air system.

In Figure 4b–d, the meniscus profiles at three locations at contact angle $\theta = 50°$ are presented, corresponding to ϕ at 141.95°, 90.64°, and 29.74° (P1, P2, and P3 denoted in Figure 4a). Through the whole process, it can be seen that the meniscus gradually changes from the initially decurved shape to an upcurved form, resulting in positive capillary force and later a negative effect on the particle. However, just like the force mentioned earlier, there are differences between the static (by analytics) and the instantaneous meniscus (by simulation) profiles in the early stage of particle motion, as shown in Figure 4b. At $\phi = 141.95°$, the particle locates closer to the fluid interface by simulation. The reason is attributed to the consideration of the dynamic process. The particle is initially in contact with the fluid interface and may be pushed down in the beginning due to the meniscus establishment. However, once the meniscus is formed quickly, the particle starts to move upward. According to Figure 4c,d, meniscus profiles gradually approach the static configuration and show good agreement with analytics as the process continues. The numerical model's validity has been demonstrated within the general water–air system and shows the advantages of dealing with dynamic processes.

4.2. Computational Analysis of Inclusion Particle Motion at Steel–slag Interface

Based on comparisons between analytical considerations and simulations above, it turns out the interaction between the particle and the water–air interface is dominated by the capillary force, and the process is featured with a quasistatic state. As for the steel–slag system of more interest here, it is expected to be quite different. As the steel–slag interface is characterized by high interfacial tension (about 20 times larger than the surface tension of the water) and high viscosity (at least 10^4 times the air viscosity), the motion of particle must deviate from a quasistatic state and is difficult to be investigated experimentally due to the high-temperature steel/slag and the small scale of inclusion size and process time. Therefore, it renders the numerical simulations a useful tool to provide insights into the mechanism of inclusion removal at the steel–slag interface.

The first case investigated is based on the parameters shown in **Table 2**. It refers to a common combination of steel and industrial slag and is considered a reference case. Within the fluids system, particle motion in the vicinity of the steel–slag interface under different wetting conditions which are distinguished by the three-phase contact angle $\theta = 10°$ and 50° is shown in **Figure 5**a. In parallel, a low-viscosity system is intentionally introduced as a comparative case where the upper fluid viscosity is $0.005\ Pa \cdot s$, as displayed in Figure 5b. For the reference case of $\theta = 10°$, the process starts with a particle initially touching the original flat interface. Then, a meniscus forms and attaches to the particle surface in a decurved way. The arrow tangent to the interface represents the surface tension effect, and its vertical component contributes to the capillary force acting on the particle. As the interface deformation further extends and evolves, the particle continues to move toward the slag side. With time, the meniscus changes into an upward form. The transition position mainly depends on the contact angle and the relative position of the sphere to the interface. At $t = 1.2 \times 10^{-4}$s shown in Figure 5a, the capillary force imposes a resistance effect on particle motion, and the net force points in the same direction at this moment. Since then, the particle hardly goes any further. It cannot get rid of the interactions with the interface and is eventually trapped at the interface. Increasing the contact angle to 50°, which indicates a deterioration of the wetting condition, the process presents slightly less interface deformation and particle movement. Accordingly, the particle ends with a lower position at the interface and with a smaller area immersed in the slag. In comparison, in the low-viscosity condition (see Figure 5b), both the interface deformation and the particle motion are particularly visible. At the three-phase contact angle of 10°, the particle is able to entirely detach from the fluid interface and be fully immersed in the top fluid. Lowering the wetting condition to $\theta = 50°$ leads to a trapped situation. In short, through the visualized motion process, it can be seen directly that high viscosity seems to result in a more rigid interface and therefore less interface deformation

Table 2. Calculation conditions of reference case.

	Density ρ [kgm^{-3}]	Viscosity μ [$Pa \cdot s$]	Interfacial tension γ_{MS} [Nm^{-1}]	Size [μm]
Steel	7000	0.005	1.2	–
Slag	2500	0.137		–
Particle	3980	–	–	50

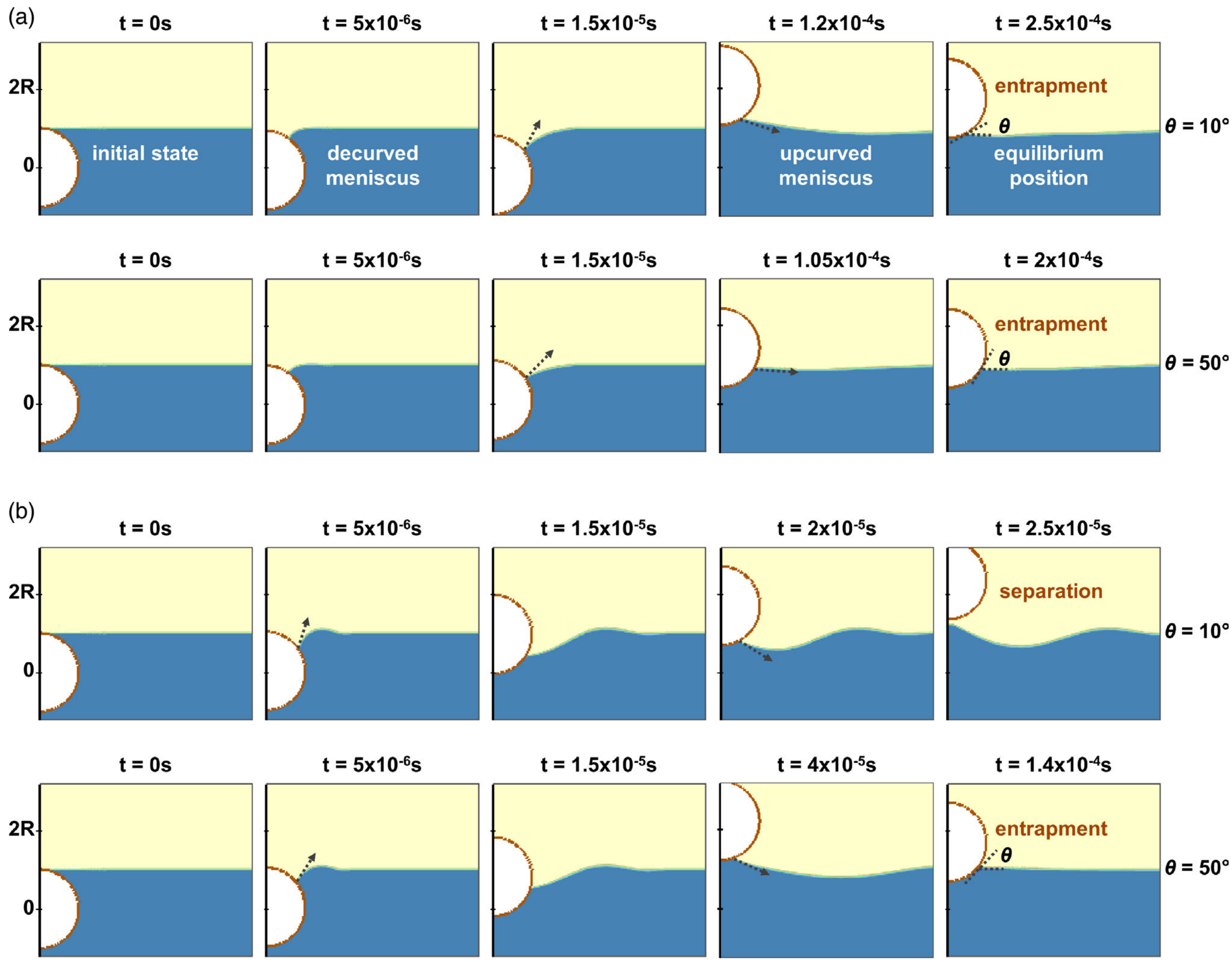

Figure 5. Process of a sphere moving across the fluid interface within (a) a reference case of steel-slag system and (b) a low-viscosity system.

and particle movement. Increasing the contact angle shows a similar effect.

During the course of motion, the force acting on the particle and the particle's velocity change with respect to its displacement are shown in **Figure 6**. Displacement represented by the horizontal axis is normalized with particle radius. The displacement always starts from zero, corresponding to the initial state where the particle is just below the interface. Following the force curve for $\theta = 10^{\circ}$ of the reference case (Figure 6a), it can be seen that the curve is to the left of zero at the beginning, and the force is negative. It indicates that a slight downward force is acting on the particle, causing it to move downward initially, approximately corresponding to the period from the initial time to $t = 5 \times 10^{-6}$s in Figure 5a. This can be related to the meniscus formation, and the system tries to reach an equilibrium state where the particle probably locates at a much lower position relative to the interface. As the meniscus is established, the force becomes positive and reaches the maximum quickly. Almost at the same moment, the particle begins to move upward from its lowest position, which corresponds to the state at $t = 1.5 \times 10^{-5}$s shown in Figure 5a. The force then gradually decreases due to a widening of the meniscus until zero and increases slightly in reverse. Meanwhile, the particle keeps moving toward the slag side up to a maximum position ($(Z/R)_{max}$ donated in Figure 6a). Although it has traveled more than one particle-diameter distance, it still cannot detach from the interface. This moment is illustrated in Figure 5a at $t = 1.2 \times 10^{-4}$s, where an upcurved meniscus still attaches to the particle bottom and tries to pull the particle back. It indicates the necessity of correlating the particle motion behavior with the interface deformation. However, as introduced before, the meniscus effect is neglected in most studies, and using particle displacement over one diameter[15] is clearly not a good separation criterion. After reaching the maximum position, due to the action of capillarity, the particle falls back and finally stays at the interface with displacement $(Z/R)_{eq}$ in Figure 6a. Similarly, the corresponding velocity–displacement curve (see Figure 6b) shows that the particle is pushed down a little bit during the initial formation of the meniscus. Then, there are typical acceleration and deceleration stages due to changes in the direction of the force. After getting

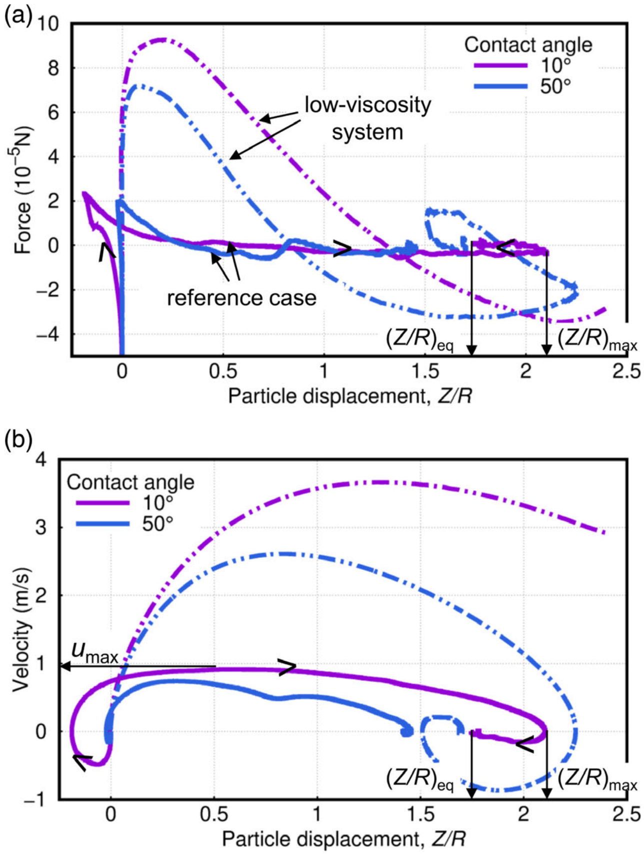

Figure 6. Particle's a) force–displacement and b) velocity–displacement curves at two different systems. $(Z/R)_{max}$ is the maximum displacement, and subscript "eq" denotes the equilibrium state.

to the maximum displacement, it moves back a certain distance and eventually is trapped at the interface. The characteristic quantities, i.e., the maximum velocity u_{max}, maximum displacement $(Z/R)_{max}$, and equilibrium position $(Z/R)_{eq}$, are also highlighted in Figure 6b. In the case of $\theta = 50°$, particle undergoes basically the same process. A few differences lie in a gentler downward movement at the beginning and smaller motion-related characteristic values. It is worth noting that the values of $(Z/R)_{max}$ and $(Z/R)_{eq}$ are very close in this case because of the stiffer interface. For the low-viscosity system, the magnitude of the characteristic quantities is overall much larger, and different wetting conditions bring a more pronounced difference. For both cases, there is no notable initial downward movement implying a more easily established interface. At $\theta = 10°$, under the action of a significant driving force, the particle gains a large velocity and reaches a high enough position to leave the interface. As the contact angle increases to 50°, particle motion is subjected to less driving force and more resistance that mainly comes from the capillary action. Consequently, it falls back with small oscillations and finally remains trapped.

The analyses above give details on the particle's motion under different wetting conditions and slag viscosity. Both factors greatly affect the characteristic values of the process. Especially the maximum velocity and the maximum displacement reflect the tendency of separation. Besides, particle motion shows a strong correlation with the interface deformation which is related to the fluid properties and the impacting particle. Therefore, a sensitivity study of particle behavior to parameters related to the three-phase system is investigated, further including the interfacial tension of the steel–slag interface (γ_{MS}), particle size (D_I), and particle density (ρ_I). The properties of the molten steel phase are not considered critical to the capillary force-driven motion, and the slag density is almost constant. Therefore, they are not included in the parameter study. It seems enough to show the impact of various parameters by only comparing the characteristic quantities, the maximum velocity $\mathbf{u}_{max}$, displacement $(Z/R)_{max}$, and final position $(Z/R)_{eq}$. Thus detailed processes and full curves are unnecessary to repeat here. For the independent variables, each parameter is varied, one at a time, within a certain range based on the reference case, and the way of analysis refers to Strandh's study.[19] As shown in **Figure 7**, variations in the slag viscosity μ_S and the interfacial tension γ_{MS} significantly affect the particle's maximum velocity. Three-phase contact angle θ and viscosity μ_S have a great influence on the maximum displacement, while the final position is mostly affected by θ. By contrast, particle size shows a minor effect on the three quantities. Particle density barely makes any difference.

Since the particle's kinetic energy is transformed by the interfacial energy, this conversion is expected to be more efficient in a less viscous environment due to the less energy dissipation, or the less viscous resistance encountered by the particle. Thus, as shown in Figure 7a, a smaller viscosity contributes to a larger maximum driving velocity. For the same considerations, increasing the interfacial tension results in a similar effect because of the increased energy source. The same explanation can be applied to the contact angle. However, according to Figure 5a, it is noticed that the fluid interface is quite stiff in the reference case and does not show a big difference between contact angles of 10° and 50°. Thus, improving the wetting condition only gives a small increase in the maximum velocity. As for the maximum displacement shown in Figure 7b, the contact angle shows a larger effect than the slag viscosity. Although the viscosity results in a significant change in the maximum velocity, the capillary force shows resistance when the particle exceeds a certain position. The capillary force also leads to the deceleration of the particle. Therefore, the maximum displacement is governed by both factors. It should be mentioned that there are no cases of separation within the range of parameter variation displayed in Figure 7. Due to the particle being unable to reach a high enough position to detach from the interface, it falls back and eventually stays at the interface. This equilibrium position is basically decided by the three-phase contact angle. Therefore, the key parameters to particle separation are those parameters that affect the maximum displacement, that is to say, 1) the wetting condition and 2) the slag viscosity, which should be considered for large-scale model development.

4.3. A Criterion for Particle Separation at Fluid–Fluid Interface

For particle motion in the vicinity of a fluid–fluid interface driven by the capillary force, two behaviors are exhibited: separation

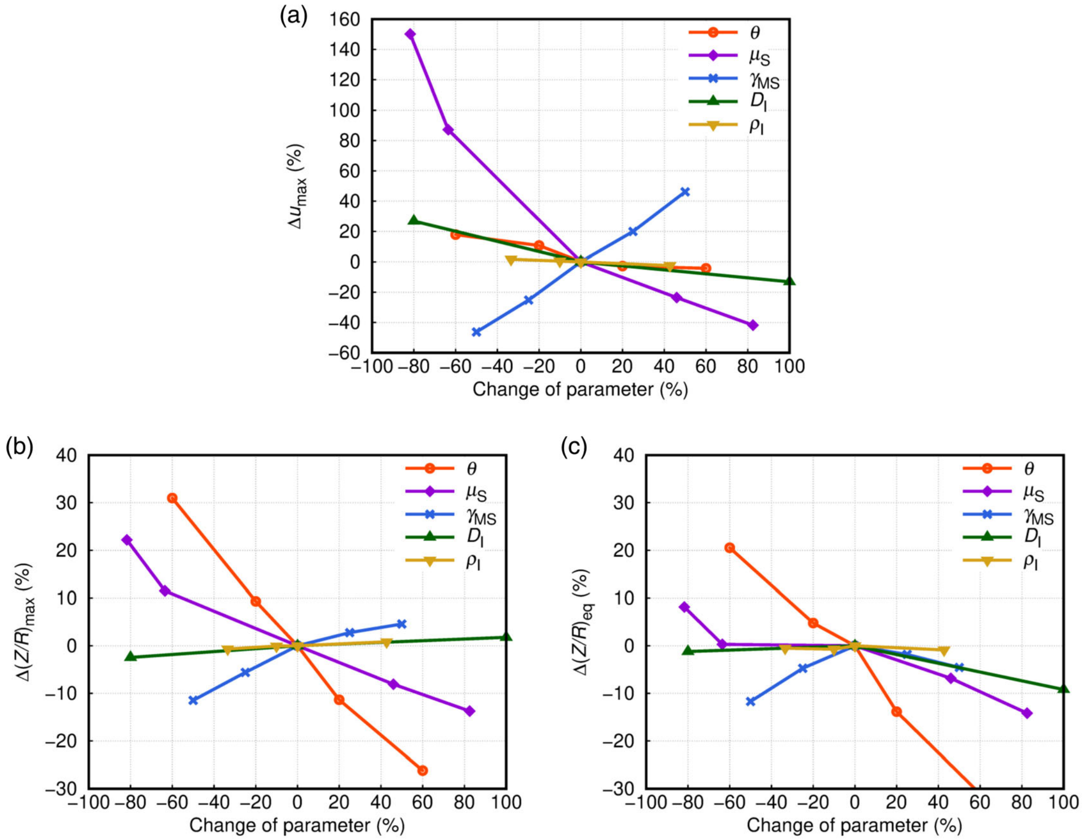

Figure 7. Effects of parameter variation on the characteristic quantities related to particle motion: a) maximum velocity $\mathbf{u}_{\max}$, b) maximum displacement $(Z/R)_{\max}$, and c) equilibrium position $(Z/R)_{\mathrm{eq}}$. The parameters considered are the three-phase contact angle θ, slag viscosity μ_S, particle size D_I, particle densityρ_I, and the interfacial tension of steel–slag interfaceγ_{MS}.

from the interface and entrapment at the interface. Within a water-air system, it is not only a capillary force-driven motion but also capillary force dominated. There is basically no energy dissipation due to the negligible viscosity of air, and interfacial energy is transformed into the particle's kinetic energy to promote particle motion. As a result, almost all hydrophobic particles can be detached from the interface. Whereas for the steel–slag system, especially for highly viscous tundish slag, the total force that drives the particle motion diminishes dramatically due to viscous dissipation. Consequently, the particle hardly gets separated and ends up entrapment at the interface in different positions. The two systems stand for two extreme situations, from capillary force dominated to capillary force and viscosity dominated. The particle behavior also transforms from separation to entrapment. In order to investigate the regime transition and develop a criterion for predicting particle behavior at the fluid interface, more simulation cases within a wide range of parameters are investigated.

All the simulation results are presented in a diagram shown in **Figure 8**. The horizontal axis is denoted by $\zeta = \rho_I \mathbf{u}_{\max}^2 D_I$, where $\mathbf{u}_{\max}$ is the particle's maximum velocity and is considered as the characteristic velocity of the process as introduced before. ζ is a quantity related to the particle dynamics. It is computed from the particle kinetic energy divided by a scale of surface area, thus having the same unit with surface energy. From a physical point of view, ζ represents the particle-contained energy that is transformed from the interfacial energy of fluids. As the investigated case is subjected to the viscous effect and the capillary action, two dimensionless numbers are employed. The Reynolds number, which has the general form $\mathrm{Re} = \rho\, \mathbf{u}\, L/\mu$, represents the ratio of inertial forces to viscous forces, while the Capillary number $\mathrm{Ca} = \mu\, \mathbf{u}/\sigma$ denotes the ratio of viscous forces to surface tension forces. Hence, Re/Ca can be used as a measure of the relative effect of the surface tension forces to the viscous forces, with negligible inertia effect in the current situation. Therefore, $\mathrm{Re/Ca} = \rho_S\, \gamma_{MS}\, D_I/\mu_S^2$ is constructed on the vertical axis. Here, it is preferred to borrow the concept of "capillary velocity,"[44,45] which is $V_{\mathrm{cap}} = \sigma/\mu$, to substitute the characteristic velocity that appears in the original form of the Reynolds number. Finally, a capillarity-related Reynolds number Re_γ ($\mathrm{Re}_\gamma = \rho_S\, \gamma_{MS}\, D_I/\mu_S^2$) is applied, which is independent of the process kinematics $\mathbf{u}_{\max}$ and only depends on the fluid properties and the geometry of interest. Re_γ also evaluates the damping effects of viscosity.

According to Figure 8, the larger Re_γ and ζ are favorable for particle separation. It indicates situations with high interfacial energy sources, high energy transfer efficiency, and less viscous dissipation. By decreasing Re_γ, the separation is subjected to the case of better wetting conditions. When the Reynolds number is below a certain value, all particles are trapped at the interface

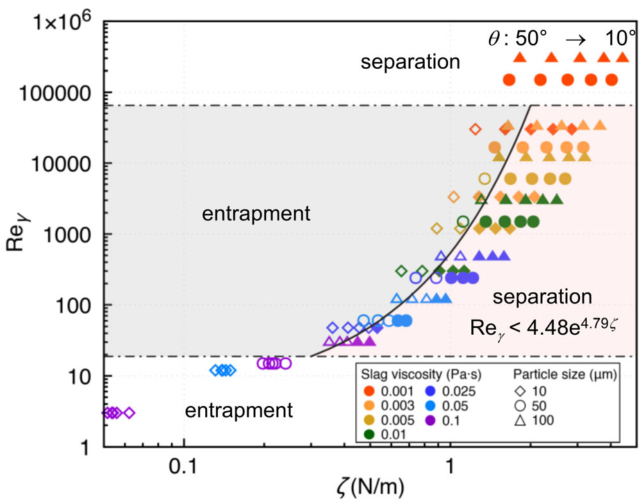

Figure 8. The Re_γ-ζ graph representing all the simulated cases in terms of particle dynamics (ζ) to the surface tension and viscous effects of fluids (reflected in Re_γ). Three critical parameters are included: slag viscosity (denoted by different colors), three-phase contact angle θ (five data points in each row denoted by θ from 50° to 10°), and particle size (denoted by different symbols). The solid curve represents the data-fitted criterion distinguishing between particle separation and entrapment, i.e., particles in the red area are separated from the interface, satisfying $Re_\gamma < 4.48e^{4.79\zeta}$. Two subregions at the top and bottom of the graph are associated with particle separation and entrapment, respectively.

almost independent of wettability. Realistic steel–slag systems usually lie in the transitional and the nonseparation region depending on the type of slag. A particle can be fully separated at a very good wetting condition for ladle and mold slags, whereas there is simply no separation for tundish slag due to the high viscosity. Current conclusions are drawn based on an analysis of the capillary-driven motion at the interface. A further investigation of the effect of flow conditions near the interface might be important. It also suggests that the validity of flow pattern optimization should be evaluated by considering the effect on particle separation at the interface. To connect the energy ζ with the flow near the interface might optimize the current criterion and make it directly useable for large-scale simulations.

5. Conclusion

In this study, the separation of a spherical particle at the steel–slag interface is investigated using the dynamic overset grid-based multiphase CFD simulation. The model validity in capturing the meniscus and accurately calculating the capillary force is first established by comparing with the analytical results. On top of that, the sensitivity of the particle behavior to the properties of the three-phase system is evaluated, and the system's wetting condition and the slag viscosity show significant effects. The results can be well interpreted from an energy point of view. This understanding further leads to the development of a general criterion for predicting particle behavior at the fluid–fluid interface. The main conclusions are summarized as follows: 1) Analyses of particle's motion process show that the effect and the magnitude of the force acting on the particle closely correlate with the meniscus shape. A decurved meniscus plays a positive role, whereas an upcurved one imposes a resistance effect on particle separation. The overall magnitude decreases in a more viscous and less wetting environment where the interface behaves more rigidly. 2) A sensitivity analysis shows that the particle dynamics are governed by the three-phase wetting angle and the fluid viscosity. Better wetting conditions and small viscosity result in larger characteristic velocity and maximum displacement, showing a better tendency for particle detaching from the interface. Within a range of parameters, two kinds of particle behaviors are exhibited: separation and entrapment. A proposed criterion for separation is given by $Re_\gamma < 4.48e^{4.79\zeta}$. 3) For steel–slag systems, especially the tundish slag, improving the wetting condition shows a limited effect on particle separation due to the highly viscous slag. The interfacial energy of fluids cannot be effectively transformed into the particle's kinetic energy. As a result, the particle tends to be trapped at the interface.

The current study provides detailed insights into the small-scale interfacial separation phenomenon. The proposed criterion based on Re_γ and ζ nicely connects the particle behavior with the system's properties. It shows the possibility of being a boundary condition to be incorporated by large-scale simulations, thus improving the existing studies on inclusion removal in metallurgical vessels.

Acknowledgements

The authors gratefully acknowledge the funding support of K1-MET GmbH, metallurgical competence center. The research program of the K1-MET competence center was supported by COMET (Competence Center for Excellent Technologies), the Austrian program for competence centers. COMET was funded by the Federal Ministry for Climate Action, Environment, Energy, Mobility, Innovation and Technology, the Federal Ministry for Digital and Economic Affairs, the Federal States of Upper Austria, Tyrol and Styria, as well as the Styrian Business Promotion Agency (SFG). In addition to the public funding from COMET, this research project was partially financed by the industrial partners (voestalpine Stahl Linz GmbH, voestalpine Stahl Donawitz GmbH, and RHI Magnesita GmbH).

Conflict of Interest

The authors declare no conflict of interest.

Data Availability Statement

The data that support the findings of this study are available from the corresponding author upon reasonable request.

Keywords

computational fluid dynamics, numerical simulations, particle separations, steel cleanliness, volume of fluid method

Received: November 3, 2022
Revised: January 26, 2023
Published online:

[1] L. Zhang, Q. Ren, H. Duan, Y. Ren, W. Chen, G. Cheng, W. Yang, S. Sridhar, *Miner. Process. Extr. Metall.* **2020**, *129*, 184.
[2] J. Nakashima, T. Toh, *Nippon Steel Tech. Rep.* **2013**, *104*.
[3] S. Lee, C. Tse, K. Yi, P. Misra, V. Chevrier, C. Orrling, S. Sridhar, A. Cramb, *J. Non Cryst. Solids* **2001**, *282*, 41.
[4] B. H. Reis, W. V. Bielefeldt, A. C. F. Vilela, *ISIJ Int.* **2014**, *54*, 1584.
[5] S. Sridhar, A. Cramb, *Metall. Mater. Trans. B* **2000**, *31*, 406.
[6] Y. Sahai, *Metall. Mater. Trans. B* **2016**, *47*, 2095.
[7] L. Zhang, S. Taniguchi, *Int. Mater. Rev.* **2000**, *45*, 59.
[8] J.-H. Park, I.-H. Jung, H.-G. Lee, *ISIJ Int.* **2006**, *46*, 1626.
[9] S. Feichtinger, S. K. Michelic, Y.-B. Kang, C. Bernhard, *J. Am. Ceram. Soc.* **2014**, *97*, 316.
[10] S. Michelic, J. Goriupp, S. Feichtinger, Y.-B. Kang, C. Bernhard, J. Schenk, *Steel Res. Int.* **2016**, *87*, 57.
[11] W. Mu, N. Dogan, K. S. Coley, *JOM* **2018**, *70*, 1199.
[12] Y. Chung, A. W. Cramb, *Metall. Mater. Trans. B* **2000**, *31*, 957.
[13] M. Saeedipour, S. Puttinger, N. Doppelhammer, S. Pirker, *Chem. Eng. Sci.* **2019**, *198*, 98.
[14] S. Puttinger, M. Saeedipour, *Exp. Comput. Multiphase Flow* **2022**, *4*, 175.
[15] K. Nakajima, K. Okamura, in *Proc. of the 4th Int. Conf. on Molten Slags and Fluxes*, ISIJ, Sendai, 8-11 June **1992**, p. 505.
[16] D. Bouris, G. Bergeles, *Metall. Mater. Trans. B* **1998**, *29*, 641.
[17] G. Shannon, S. Sridhar, in *Proc. of 2005 TMS Annual Meeting*, San Francisco, CA, 13-17 February **2005**, p. 307.
[18] J. Strandh, K. Nakajima, R. Eriksson, P. Jönsson, *ISIJ Int.* **2005**, *45*, 1838.
[19] J. Strandh, K. Nakajima, R. Eriksson, P. Jönsson, *ISIJ Int.* **2005**, *45*, 1597.
[20] C. Liu, S. Yang, J. Li, L. Zhu, X. Li, *Metall. Mater. Trans. B* **2016**, *47*, 1882.
[21] D. Vella, *Annu. Rev. Fluid Mech.* **2015**, *47*, 115.
[22] F. Schellenberger, P. Papadopoulos, M. Kappl, S. A. Weber, D. Vollmer, H.-J. Butt, *Phys. Rev. Lett.* **2018**, *121*, 048002.
[23] Y. Tang, S. Cheng, *Phys. Rev. E* **2018**, *98*, 032802.
[24] C. Xuan, E. S. Persson, R. Sevastopolev, M. Nzotta, *Metall. Mater. Trans. B* **2019**, *50*, 1957.
[25] H. Maru, D. Wasan, R. Kintner, *Chem. Eng. Sci.* **1971**, *26*, 1615.
[26] M. Manga, H. Stone, *J. Fluid Mech.* **1995**, *287*, 279.
[27] A. Geller, S. Lee, L. Leal, *J. Fluid Mech.* **1986**, *169*, 27.
[28] N. Dietrich, S. Poncin, H. Z. Li, *Exp. Fluids* **2011**, *50*, 1293.
[29] M. Javurek, R. Wincor, *Steel Res. Int.* **2020**, *91*, 2000415.
[30] M. Saeedipour, S. Pirker, *Steel Res. Int.* **2022**, 2100800.
[31] B. G. Thomas, *Steel Res. Int.* **2018**, *89*, 1700312.
[32] W. Liu, J. Liu, H. Zhao, S. Yang, J. Li, *Metall. Mater. Trans. B* **2021**, *52*, 2430.
[33] X. Zhang, S. Pirker, M. Saeedipour, *Exp. Comput. Multiphase Flow* **2022**, *4*, 178.
[34] H. Lamb, *Statics: Including Hydrostatics and the Elements of the Theory of Elasticity*, The University Press, Cambridge **1924**.
[35] A. Rapacchietta, A. Neumann, *J. Colloid Interface Sci.* **1977**, *59*, 555.
[36] A. V. Nguyen, H. J. Schultze, *Colloidal Science of Flotation*, CRC Press, Boca Raton **2003**.
[37] C. W. Hirt, B. D. Nichols, *J. Comput. Phys.* **1981**, *39*, 201.
[38] J. U. Brackbill, D. B. Kothe, C. Zemach, *J. Comput. Phys.* **1992**, *100*, 335.
[39] D. Snyder, E. Koutsavdis, J. Anttonen, in *Proc. of 33rd AIAA Fluid Dynamics Conference and Exhibit*, Orlando, Florida, 23-26 June **2003**, p. 3919.
[40] A. Khaware, V. K. Gupta, K. Srikanth, M. Azhar, in *Proc. of the 4th World Congress on Momentum, Heat and Mass Transfer*, Rome, Italy, 10-12 April **2019**, p. 10.
[41] A. Wang, Q. Song, Q. Yao, *Atmos. Environ.* **2015**, *115*, 1.
[42] J. M. Aristoff, J. W. Bush, *J. Fluid Mech.* **2009**, *619*, 45.
[43] O. Pitois, X. Chateau, *Langmuir* **2002**, *18*, 9751.
[44] G. H. McKinley, *SOR Bull.* **2005**, *74*, 6.
[45] J. Eggers, *Rev. Mod. Phys.* **1997**, *69*, 865.